



Influence of Deep Cryogenic Treatment and Secondary Tempering on Microstructure and Mechanical Properties of Medium-Carbon Low-Alloy Steels

Wanglin Chen, Weikai Wu, Cong Li, and Xianna Meng

(Submitted June 21, 2018; in revised form October 23, 2019; published online January 2, 2020)

Deep cryogenic treatment (DCT) and secondary tempering for 40CrNiMoA steel were carried out to obtain the desirable microstructures corresponding to excellent mechanical properties suiting for the preparation of flex spline of harmonic drive reducer. The effects of DCT and secondary tempering on microstructural characteristics and mechanical properties were investigated by x-ray diffraction, scanning electron microscopy, electron backscattered diffraction and transmission electron microscopy, in association with property measurements. The results show that the DCT promotes the transformation of retained austenite to martensite, the precipitation and homogeneous distribution of carbides as well as the refinement of martensitic substructures. The structural and morphological changes significantly improve the hardness, yield and tensile strength of steels, but slightly lower the elongation of them. Further secondary tempering at special temperatures can successively increase the elongation and fracture toughness of the DCT-treated 40CrNiMoA steels at the cost of slight decrease in hardness and strength due to the reduction in dislocation density. Therefore, the DCT in combination with secondary tempering can improve the comprehensive mechanical properties of 40CrNiMoA steels to produce the flex spline with a higher lifetime.

Keywords 40CrNiMoA steel, carbide, deep cryogenic treatment, martensitic structure, phase transformation

1. Introduction

As a new type of gearing transmission, the harmonic drive reducer has the higher compactness, the lighter weight, the higher transmission ratio and transmission accuracy when compared with the traditional gearing transmission (Ref 1). Thus, it has been widely used in the fields of aerospace and industrial robots (Ref 1). Flex spline, being one of key components of harmonic drive reducer, should have high precision, high torsional rigidity of output, abrasion resistance and anti-fatigue. To satisfy these performance requirements, the vacuum-heat-treated ultra-pure bearing steels were commonly carried out to produce the flex spline.

As one of the typical ultra-pure bearing steels, the quenched and tempered (QT) 40CrNiMoA steels show high strength and fracture toughness and therefore are used widely to produce kinds of axles, fasteners, traditional gears and turbine shafts. In

industrial applications, the 40CrNiMoA steels have been also carried out to produce the flex spline, but it is unclear whether or not conventional QT-treated 40CrNiMoA steels are suitable for the preparation of flex spline due to that the corresponding data belongs to trade secrets.

Deep cryogenic treatment (DCT) at liquid nitrogen temperature ($-196\text{ }^{\circ}\text{C}$) is a supplementary process to conventional heat treatment before tempering (Ref 2). In past decades, the DCT has been applied mainly in high-speed steels, stainless steels and die steels (Ref 3–8). It has been demonstrated that the DCT does not only give dimensional stability to the components, but also improves mechanical properties such as hardness, wear resistance and fatigue strength (Ref 9–12). In general, the mechanisms to improve the mechanical and tribological properties of steels are closely associated with the transformation of retained austenite to martensite (Ref 13, 14), as well as the precipitation and distribution of fine carbides (Ref 15). Although a few investigations on the DCT effect have been reported regarding carbon steels (Ref 2), the investigations on microstructures in more details are limit, and the relationships among the heat treatment methods, microstructures and mechanical property are not understood well.

In present work, we systematically study aforementioned relationships by x-ray diffraction (XRD), scanning electron microscopy (SEM), electron backscattered diffraction (EBSD) and transmission electron microscopy (TEM), in association with property measurements. Our results show that the DCT is introduced to promote the transformation of retained austenite to martensite, the refinement of martensitic substructure, precipitation and homogeneous distribution of carbides, but does not affect grain size of prior austenite. Secondary tempering at special temperatures (lower than first tempering temperature) almost does not affect the microstructure features beside dislocation density within the martensitic laths. As a result, the DCT enhances the yield strength, tensile strength and

Wanglin Chen and **Weikai Wu**, School of Electromechanical Engineering, Guangdong University of Technology, Guangzhou City, Guangdong Province 510006, People's Republic of China; **Cong Li**, School of Energy and Power Engineering, Changsha University of Science and Technology, Changsha, Hunan Province 410083, People's Republic of China; and **Xianna Meng**, School of Mechanical and Automotive Engineering, South China University of Technology, Guangzhou City, Guangdong Province 510006, People's Republic of China. Contact e-mails: chenlin1038@163.com and mengna_yu@126.com.

fracture toughness of 40CrNiMoA steel, and to further ensure the long lifetime of flex spline. DCT in combination with secondary tempering at special temperatures can obtain much more excellent comprehensive mechanical properties.

2. Materials and Experimental Procedure

2.1 Material Preparation

A commercial 40CrNiMoA steel, with chemical compositions of 0.44 wt.% C, 0.86 wt.% Cr, 0.20 wt.% Mo, 1.72 wt.% Ni, 0.78 wt.% Mn, 0.26 wt.% Si, 0.02 wt.% P, 0.01 wt.% S and balance for Fe, was supplied in normalized condition. In order to evaluate the DCT effect, conventional QT method was used as a reference. In this case, several groups of samples were subjected to the QT method including: austenitizing at 830-860 °C for 30 min in a tube furnace under flowing nitrogen atmosphere, followed by oil quenching at room temperature, and finally tempered at 550-600 °C for 2 h.

The DCT treatment consisted of oil-quenched samples at room temperature to about -30 °C for 3 h, and then to -196 °C for 24 h, and finally bring the samples back to room temperature. The DCT treatment was performed directly after oil quenching at room temperature, and followed by tempering treatment. In order to obtain desirable microstructures and mechanical properties, some quenched samples were tempered for twice. In this work, different heat treatment sequences were used to evaluate the response of 40CrNiMoA steel to cryogenic treatment (Table 1).

2.2 Measurement Methods

The standard dimensions for tensile test and Charpy impact test were machined according to the ASTM E 517-00 and ASTM E 23, respectively. The tensile experiments were performed on an Instron 3369 machine controlled under a constant crosshead of 3 mm/min until fracture, and the Charpy V-noted experiments were employed by an Instron Dynatup 9200 weight impact tester at room temperature (25 °C). The hardness values of all tested

samples were measured by a Vickers hardness tester with a load of 500 g, and each hardness value is an average value of five test points. The loading, dwelling and unloading time for Vickers hardness tests was 15 s, respectively. The lifetime of harmonic drive reducer was tested by our self-made test equipment at room temperature, and corresponding schematic diagram was shown in the literature (Ref 16). Specific parameters including harmonic drive reducer and test equipment are not shown here due to the business secrecy, and only finally lifetimes are given out in the present work.

Prior to microstructural characterizations, all samples were ultrasonically cleaned in ethanol. A Bruker D8 advance x-ray diffractometer operating with Cu K α radiation with vanadium filters at 50 kV and 150 mA was used for phase analysis. The scans recorded in the range of 30°-100° with a step of 0.02° and a dwelling time of 0.5 s. The volume fraction of retained austenite were estimated according to the ASTM standard E975-00 (Ref 17), considering the {200}, {220} and {311} crystal planes of retained austenite and {200}, {211} and {220} crystal planes of martensite. A FEI Nano 430 scanning electron microscopy (SEM) equipped with a Nordlys Nano Oxford detector of electron backscattered diffraction (EBSD) operating at a voltage of 20 kV was used for microstructural analysis in more details. Then, EBSD mapping was processed by the standard EBSD processing software to obtain the prior austenitic grain size and packet size. At least 100 prior austenite grains and 300 packets were used for statistically measuring size. At less fifteen TEM images were used to determine the average width of martensitic laths in each tested sample by Photoshop software. The samples for SEM observations were first mechanically polished and then etched with 5% nital solution for 15 s. The contents of carbides were roughly measured by combination of Photoshop software and OM analysis software. A JEM 2010 transmission electron microscopy (TEM) equipped with an EDS operating at 200 kV was performed for microstructural examinations in more details. The TEM samples were first prepared by mechanical polishing and then by electro-polishing with solution of 10 vol.% perchloric + 90 vol.% acetic acid at room temperature with an applied voltage of 35 V.

Table 1 Detailed heat treatment processes of tested samples and corresponding hardness

Names	Heat treatment				Hardness, HV
	Quenching temperature, °C	DCT	1st tempering	2nd tempering	
A	850 °C×0.5 h	No	No	No	561.2 ± 5.6
B	830 °C×0.5 h	No	580 °C×2 h	No	313.6 ± 3.2
C	850 °C×0.5 h	No	580 °C×2 h	No	308.7 ± 2.8
D	880 °C×0.5 h	No	580 °C×2 h	No	302.9 ± 2.2
E	850 °C×0.5 h	Yes	No	No	584.6 ± 5.1
F	830 °C×0.5 h	Yes	580 °C×2 h	No	341.4 ± 3.1
G	850 °C×0.5 h	Yes	580 °C×2 h	No	336.2 ± 3.2
H	880 °C×0.5 h	Yes	580 °C×2 h	No	332.1 ± 2.1
I	830 °C×0.5 h	Yes	600 °C×2 h	No	286.7 ± 2.2
J	830 °C×0.5 h	Yes	580 °C×2 h	580 °C×2 h	312.4 ± 2.8
K	830 °C×0.5 h	Yes	580 °C×2 h	540 °C×2 h	327.7 ± 3.4
L	850 °C×0.5 h	Yes	580 °C×2 h	580 °C×2 h	309.4 ± 2.9
M	850 °C×0.5 h	Yes	580 °C×2 h	540 °C×2 h	329.4 ± 2.4

Table 2 YS, UTS, EL and fracture toughness of the tested samples

Names	YS, MPa (Experimental value)	UTS, MPa	EL, %	A _{kv} , J
B	919.2 ± 7.1	1012.4 ± 9.2	18.4 ± 0.9	37.2 ± 2.1
C	909.5 ± 8.6	1009.2 ± 9.3	17.3 ± 1.0	33.2 ± 2.4
D	901.6 ± 8.4	1002.9 ± 9.2	17.0 ± 1.1	29.5 ± 1.7
F	988.8 ± 6.9	1066.6 ± 8.8	16.9 ± 1.2	33.4 ± 1.4
G	965.8 ± 7.3	1052.6 ± 8.9	16.3 ± 1.3	30.1 ± 2.0
J	881.4 ± 7.8	968.7 ± 7.1	18.4 ± 1.3	78.3 ± 2.1
K	950.8 ± 8.2	1045.3 ± 8.2	17.0 ± 0.9	36.5 ± 1.8
M	969.1 ± 7.7	1049.1 ± 9.4	17.3 ± 1.5	40.8 ± 1.9

3. Results

3.1 Property Measurements

According to the stress–strain curves of experimental samples, Table 2 shows the yield strength (YS), ultimate tensile strength (UTS) and elongation (EL) of them. As can be seen, for the un-DCT-treated samples (B, C and D), with the increase in quenching temperature from 830 to 880 °C, the YS and UTS are slightly decreased from 919.2 ± 7.1 to 901.6 ± 8.4 MPa and from 1012.4 ± 9.2 to 1002.9 ± 9.2 MPa, respectively, and simultaneously the EL is slightly decreased from 18.4 ± 0.9 to 17.0 ± 1.1%. After the DCT, the YS of both F- and G-samples is increased to 988.8 ± 6.9 and to 965.8 ± 7.3 MPa, and their corresponding UTS are also increased to 1066.6 ± 8.8 and to 1052.6 ± 8.9 MPa, but the EL is somewhat decreased. For the J-sample, its YS and UTS are decreased to 881.4 ± 7.8 and to 968.7 ± 7.1 MPa, much lower than those (969.1 ± 7.7 and 1049.1 ± 9.4 MPa) of M-sample, but its EL is slightly improved.

The effects of DCT and secondary tempering on impact energy have been carried out, and corresponding measured results are also in Table 2. It can be found that the impact energies of B- and C-samples are 37.2 ± 2.1 and 33.2 ± 2.4 J, whereas the ones of F- and G-samples are 33.4 ± 1.4 and 30.1 ± 2.0 J, respectively. This indicates that DCT-treated samples show the lower fracture toughness when compared with the QT-treated samples. For the secondary tempered samples, the impact energies of M-, K- and J-samples increased to 40.8 ± 1.9, 36.5 ± 1.8 and 78.3 ± 2.1 J, respectively. This indicates that the secondary tempering can increase the fracture toughness of DCT-treated samples.

3.2 Microstructural Characterizations

3.2.1 XRD Analysis. Conventional XRD method was carried out to identify the retained austenite of tested samples (named as A, C and E in Table 1), and corresponding results are shown in Fig. 1. As can be seen, compared to the A-sample, the diffraction peaks from the retained austenite (γ -phase) of the E-sample have been weakened substantially. Further calculated results show that the volume fraction of retained austenite in A-sample is about 6.2%, and after the DCT, the one in E-sample is rapidly reduced to about 3.5%. This indicates that the DCT can effectively induce the phase transformation of retained austenite to martensite, resulting in an increase in hardness from 561.2 ± 3.6 to 584.6 ± 4.1 HV (Table 1), but

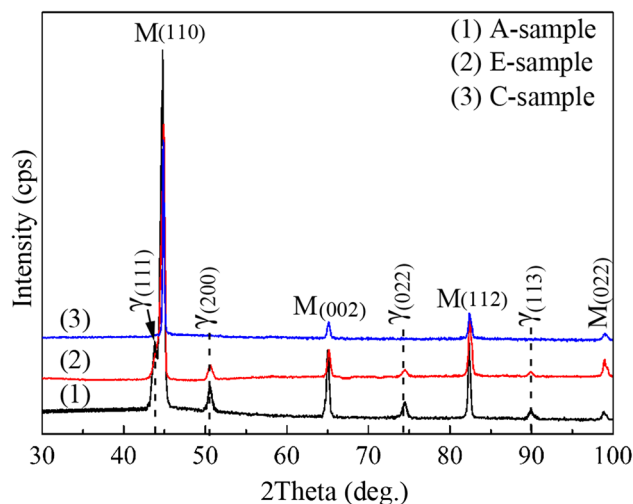


Fig. 1 Typical XRD patterns of A-, C- and E-samples

this phase transformation is incomplete. For the QT-treated sample (C-sample) with DCT, only diffraction peaks from martensitic structure are observed (Fig. 1), indicating that the retained austenite has completely transformed into tempered martensite during the tempering process, resulting in a notable loss in hardness from 584.6 ± 4.1 to 308.7 ± 2.8 HV.

3.2.2 The Effect of DCT on Microstructure. It has been demonstrated that according to crystallographic features, the lath martensitic microstructures can be generally described by the descending levels of prior austenite grain, packet, block and lath. A prior austenitic grain commonly consists of some martensitic packets with the same habit plane exhibits, and each packet is composed of martensitic blocks with the same orientation, and each block is composed of several martensitic laths (Ref 18). It has been reported that the strength is inversely proportional to grain sizes of prior austenite or packet size (Ref 19). Therefore, structure evolutions during the heat treatment processes can directly reflect the changes in mechanical properties.

Figure 2 shows typical EBSD orientation maps of QT samples without DCT (named as D-, C- and B-samples in Table 1). The primary austenite indeed consists of several martensitic packets. The average grain sizes of prior austenite of the D-, C- and B-samples are 15.2 μm (Fig. 2a), 13.1 μm (Fig. 2b) and 11.3 μm (Fig. 2d), respectively, and the corresponding martensitic packet sizes are 4.54, 3.37 and 2.59 μm ,

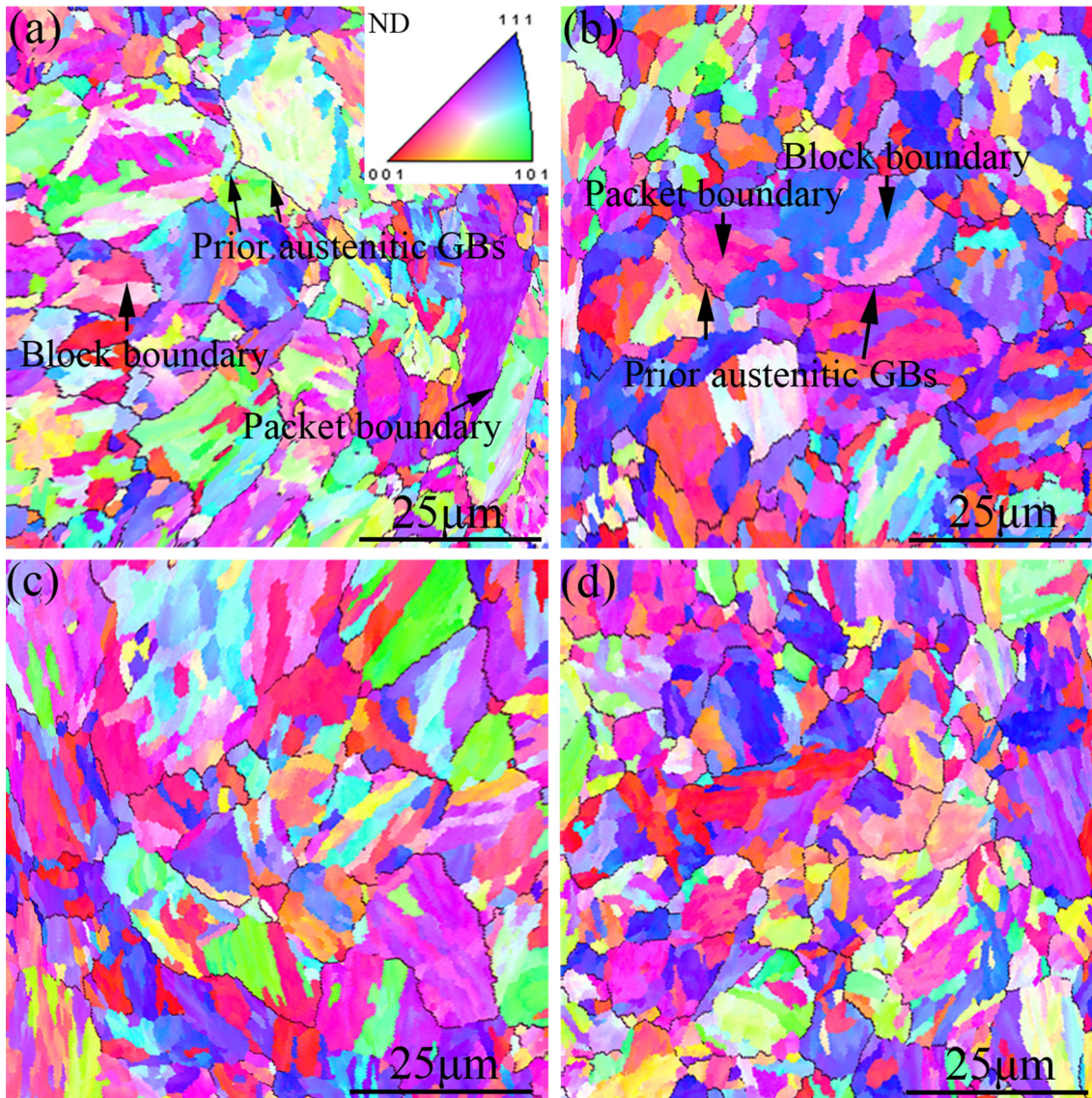


Fig. 2 Typical orientation imaging maps (inverse pole figure (IPF) [001] color maps obtained from EBSD analysis) of lath martensitic structure in tested samples: (a) D-sample; (b) C-sample; (c) G-sample; (d) B-sample. Note that black lines in maps show the prior austenite grain boundaries (GBs) with mis-orientation angles larger than 15° (Color figure online)

respectively. The grain sizes of both primary austenite and martensitic packet increased with the quenching temperature increase, indicating that the quenching treatment at 830 or 850 °C is beneficial for obtaining the finer grain sizes in comparison to quenching treatment at 880 °C. Both the G-sample and C-sample have the same quenching and tempering process, and grain sizes of prior austenite of them are basically the same, but the packet size ($2.57 \mu\text{m}$) of the G-sample is much smaller than that ($3.37 \mu\text{m}$) of the C-sample. This indicates that the DCT promotes the refinement of martensitic packets.

Compared with the tempered martensitic matrix, the carbides show much better corrosion resistance against 3.5% nital solution. So in SEM images, the carbides and the martensitic matrix should show the bright contrast image and the gray contrast image, respectively, and therefore can be directly distinguished in SEM images.

In order to roughly calculate the carbide percentage, the samples were etched deeply, and the corresponding SEM and binary images are shown in Fig. 3. It can be seen that for the QT samples with and without DCT (taking the C-sample and G-sample for example), the carbide percentage in C-sample (Fig. 3a and b) is about 1.11%, lower than that (2.98%) in G-sample (Fig. 3c and d). In addition, careful observation shows that some fine carbides combine to form long-chain-like carbides with approximately parallel direction with each other (as shown the elliptic regions in Fig. 3d). The similar method was also used to measure the carbide percentages in the other tested samples. Corresponding results demonstrate that the percentages of carbide percentages in B- and D-samples are successive 1.09 and 1.12%, whereas the ones in F- and H-samples are 2.95 and 3.08%, respectively. Obviously, regarding the samples with the same quenching and tempering processes, the DCT-treated samples always contain the higher carbide

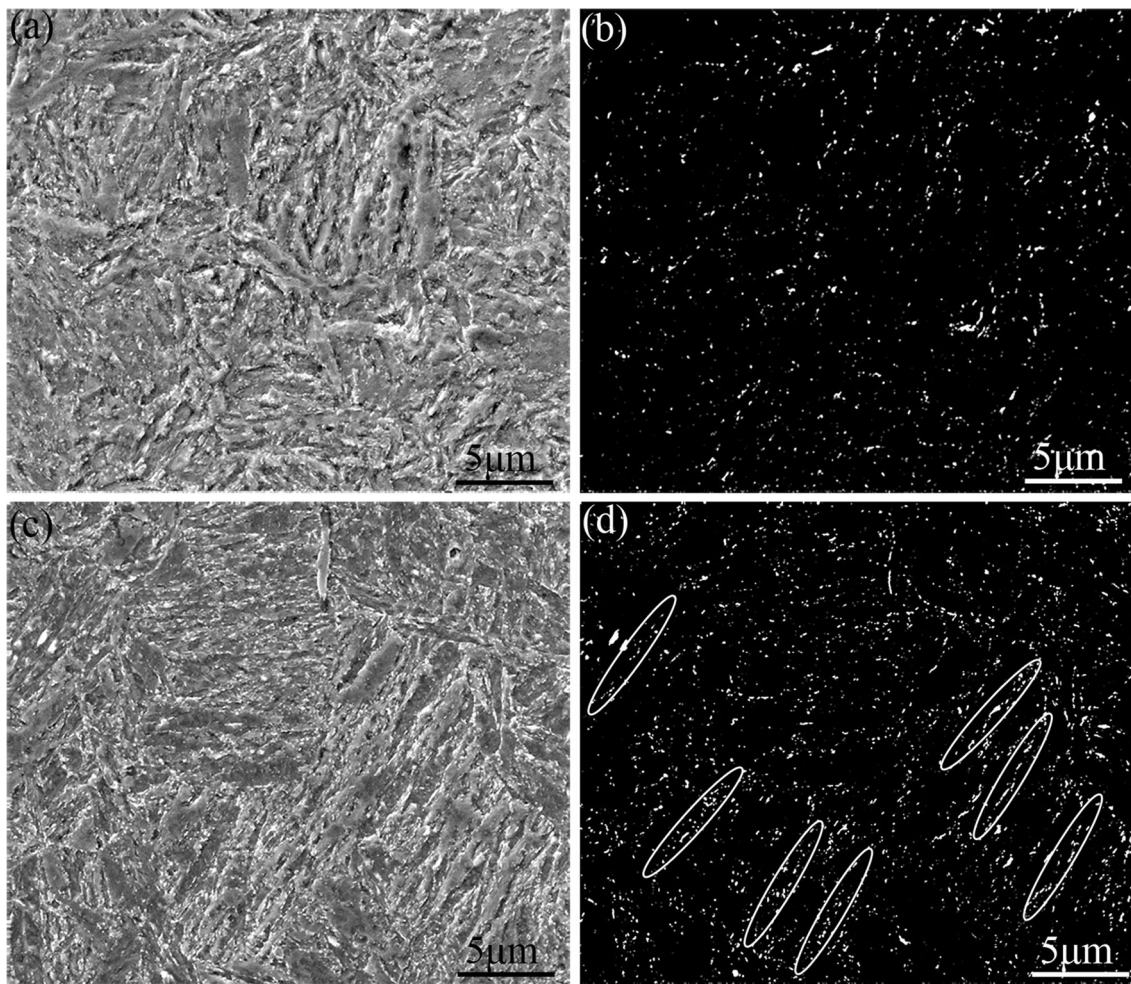


Fig. 3 Typical SEM and binary images for image analysis of tested samples quenched at 850 °C and tempered at 580 °C: (a) SEM image, C-sample; (b) binary image of (a); (c) SEM image, G-sample; (d) binary image of (c)

percentages when compared with un-DCT-treated samples. Moreover, it can be found that the distributions of carbides in DCT-treated samples are much more homogeneous when compared with the un-DCT-treated ones. It is claimed that during the DCT process, structure shrinkage at ultra-low temperature and notable difference in expansion coefficient between retained austenite and martensite produce a high degree of stresses. Such high stresses force the interstitial carbon atoms to migrate into the neighboring defects such as dislocations or phase interfaces. The migrated carbon atoms provide preferentially new sites for the carbide nucleation in subsequent tempering (Ref 10). Hence, the DCT-treated sample shows higher carbide percentage and more homogeneous distribution of carbides when compared with un-DCT-treated sample.

Figure 4 further shows typical morphologies of carbides in un-DCT- and DCT-treated samples (taking the C- and G-samples for example). It can be seen that the carbides in G-sample (Fig. 4b) are much smaller when compared with the C-sample (Fig. 4a), and its distribution is indeed more homogeneous (Fig. 4b). The even sizes of the carbides for C-sample and G-sample are 0.11 and 0.06 μm, respectively. Figure 4(c) further shows a typical EDS spectrum of a carbide particle. It shows that the carbide contains about 30.4 at.% C, 3.1 at.% Cr, 2.2 at.% Mn and the balance for Fe, and its selected-area

electron diffraction pattern (SAEDP, Fig. 4d) certifies that the carbide corresponds to cementite, also called as alloying cementite (θ - $(\text{Fe,Cr,Mn})_3\text{C}$), without exceptions. Such dispersed carbides can impede the dislocation movement by following the interaction mechanism of shearing or bypassing, resulting an increase in strength (Ref 20).

To study the effect of DCT on substructures of the tempered martensite, the un-DCT-treated B and DCT-treated F-samples were carried out, and corresponding results are shown in Fig. 5. It can be seen that the B-sample has an average block width of 2.08 μm (Fig. 5a), whereas the F-sample has a much smaller average block width of 1.12 μm (Fig. 5b). TEM observations further demonstrate that the laths in F-sample are much more straight compared to the B-sample. The average width of martensitic laths in B-sample is about 0.72 μm, the bigger than that (0.33 μm) in F-sample (Fig. 5c). The refinement of martensitic substructures (martensitic laths and their subunits) should be related to the decomposition of martensite and the formation of superfine carbides during the tempering after DCT. High stresses, caused by martensitic shrinkage at ultra-low temperature and different expansion coefficient between the retained austenite and martensite, enforce carbon atoms to segregate at dislocation lines, and finally become the boundaries of new subunits in martensitic laths (Ref 21). Thus, the martensitic laths are refined after DCT and tempering.

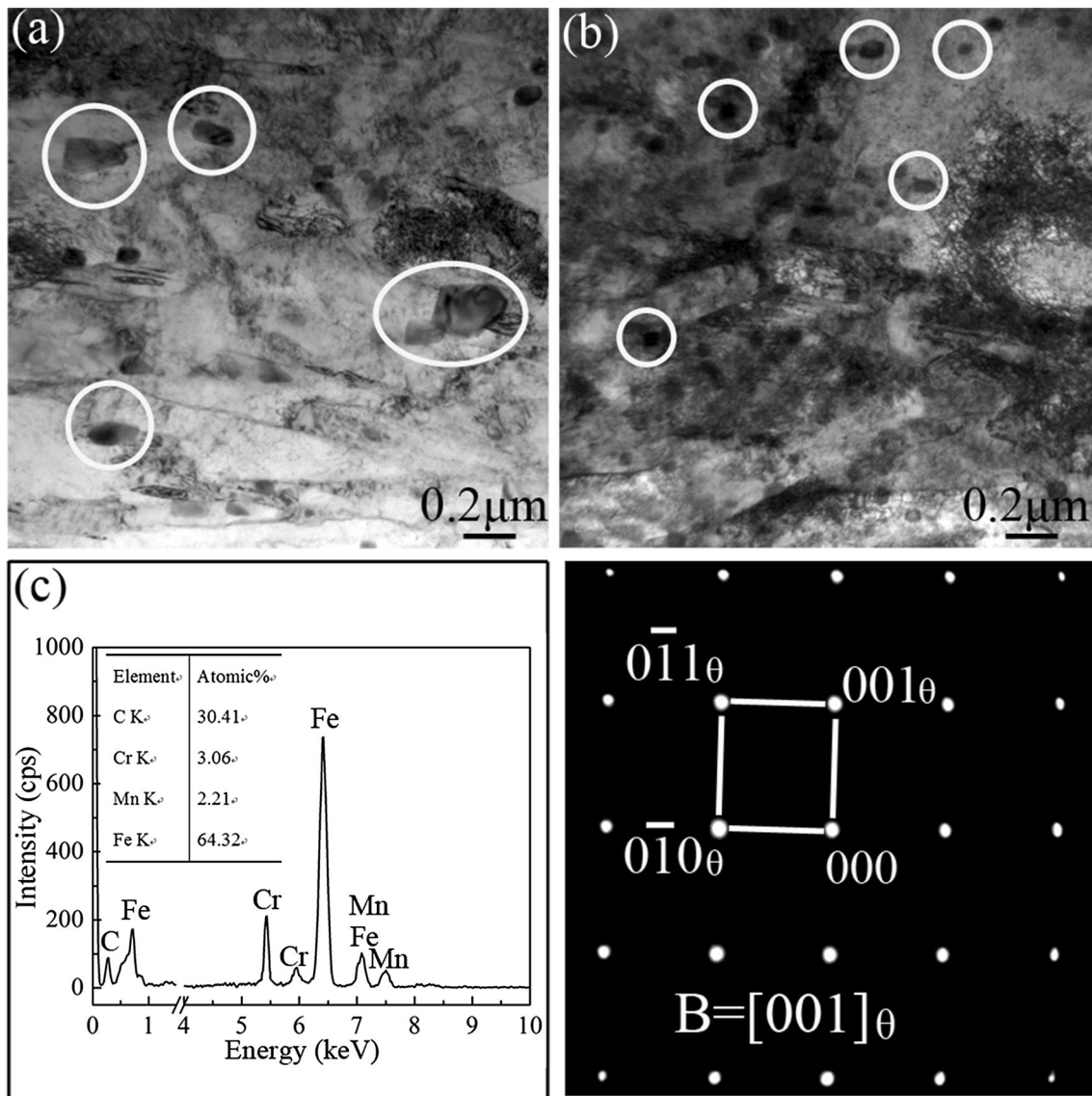


Fig. 4 Typical TEM morphologies, chemical composition and SAEDP of carbides in tested samples (C and G) quenched at 850 °C and tempered at 580 °C: (a) TEM image, no DCT; (b) TEM image, no DCT; (c) EDS; (d) SAEDP

3.2.3 The Effect of Tempering Temperature on Microstructures. During the tempering of quenched steels, the segregation of carbon, the precipitation of carbides, the decomposition of retained austenite and the recovery and recrystallization of the martensitic structure occur simultaneously (Ref 22, 23). These structural and morphological changes can simultaneously bring about the softening and hardening in tempering process. The former is related to the recovery of lath martensitic structure and dislocation, and the latter is associated with the decomposition of retained austenite, the dissolution of supersaturated carbon and the precipitation of carbides.

When the tempering temperature is no more than 580 °C, tempered samples basically show typical tempered martensitic structures, without notable differences in microstructural and morphological features. Therefore, only the microstructures of the sample tempered at 580 °C are shown here. For comparison, the sample tempered at 600 °C is also shown. Figure 6 shows the typical SEM images of the samples tempered at 580 and 600 °C. As can be seen, the sample tempered at 580 °C (F-

sample) mainly shows the typical tempered martensitic structure consisting of martensitic lath and carbides (Fig. 6a and b), whereas the sample tempered at 600 °C (I-sample) consists of lath martensitic structure, polygonal grains with irregular grain boundaries (GBs, as shown the framed zone in Fig. 6c) and equiaxed grains (as shown the elliptic zones in Fig. 6c). Further careful observation in Fig. 6(d) reveals that the polygonal grain is formed by merging of martensitic laths due to the dislocation motions during the tempering process. The appearance of equiaxed grains indicates that the recrystallization has occurred, accompanied by a notable reduction in dislocation density. Obviously, the formation of polygonal and equiaxed grains inevitably results in a notable loss in strength due to the coarsening of martensitic laths and the reduction in dislocation density.

Further TEM characterizations show that original martensitic laths indeed begin to disappear (Fig. 7a), and to transform to polygonal grains (Fig. 7b) containing some dislocation cells with irregular morphologies, and they frequently display low

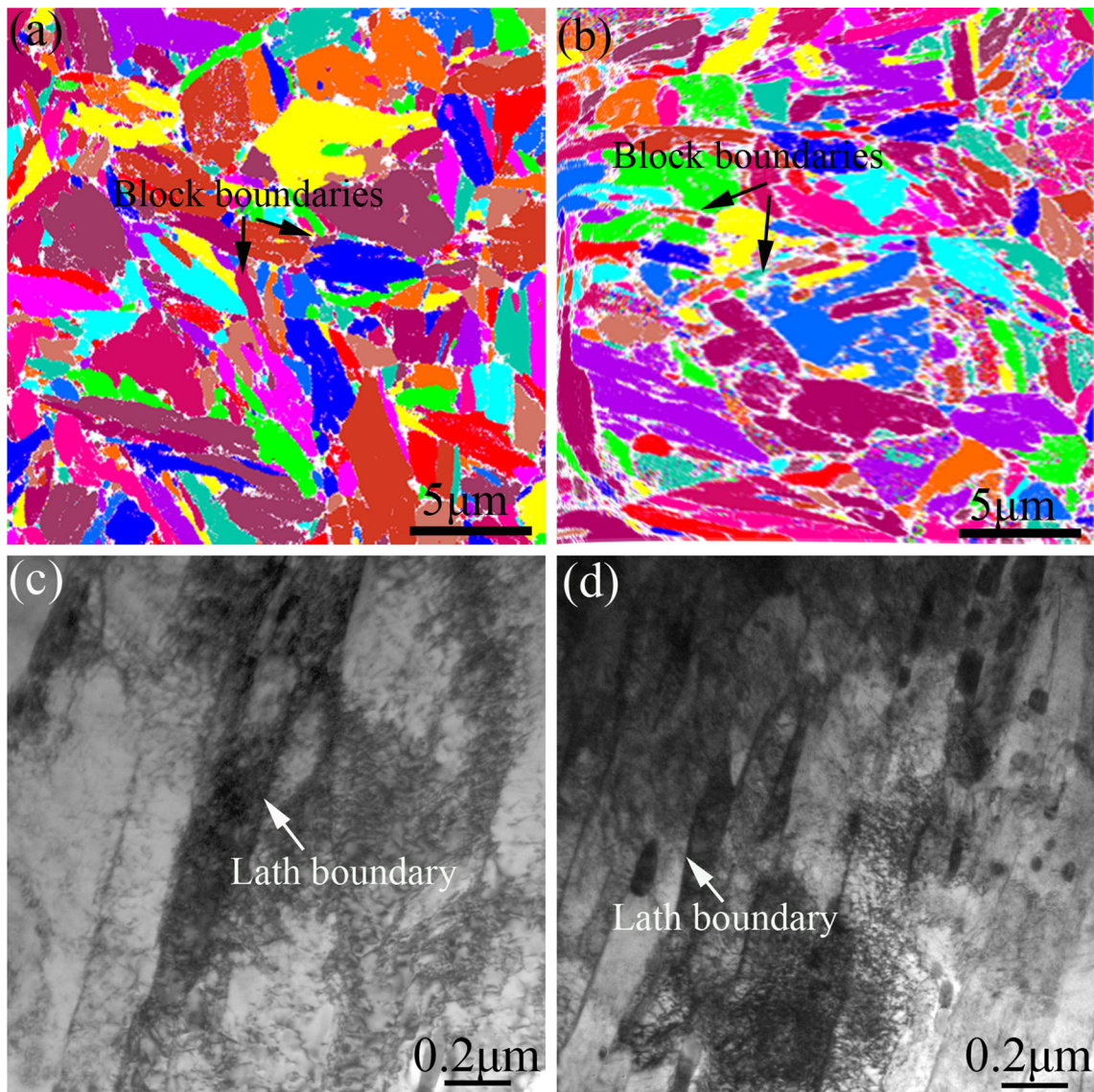


Fig. 5 Typical morphologies of martensitic laths in tested samples: (a) IPF [001] color map, B-sample; (b) IPF [001] color map, F-sample; (c) TEM image, B-sample; (d) TEM image, F-sample (Color figure online)

dislocation density inside but high outside. Meanwhile, it shows that some martensitic laths begin to merge into a polygonal grain by dislocation motions (Fig. 7c). In some other zones, some equiaxed grains appear (Fig. 7d and f). Structure features of TEM observations are well consistent with findings of SEM observations. The carbides are coarsened when compared with the B-sample or F-sample, which is due to higher tempering temperature.

It is well known, when compared with the tempered martensite, both polygonal and equiaxed grains are the softer. Hence, under high external stress conditions, the plastic deformation preferentially occurs in both polygonal and equiaxed ferritic grains, resulting in local stress concentration and follow-up local necking, and eventually resulting in decohesion at ferritic/martensitic interfaces (Ref 24). Moreover, the coarsening of carbides also results in a loss in mechanical properties. Therefore, the tempering temperature should be not more than 580 °C to obtain uniform structures, and further to ensure excellent mechanical properties.

3.2.4 Effect of Secondary Tempering on Microstructures of DCT-Treated Samples.

Secondary tempering has been commonly carried out to improve the mechanical properties by adjustment of internal stress and by eliminating the retained austenite, especially in high alloy steels (Ref 9, 25). However, the findings in the present work have shown that the retained austenite in DCT-treated 4340 steel is negligible. Therefore, here the secondary tempering temperature at no more than first tempering temperature is mainly used to adjust the distribution of dislocations within martensitic laths and internal stress, and further increase the fracture toughness of the materials.

Figure 8 reveals the typical SEM images of tested samples (K- and J-samples) via twice tempering processes. As shown in Fig. 8(a), when the first and the secondary tempering are both carried out at 580 °C (J-sample), some typical martensitic laths begin to transform into fine polygonal grains with elongated morphologies. Figure 8(b) further demonstrates that these polygonal grains are mainly formed by martensitic lath merging. When the temperatures of the first and the secondary

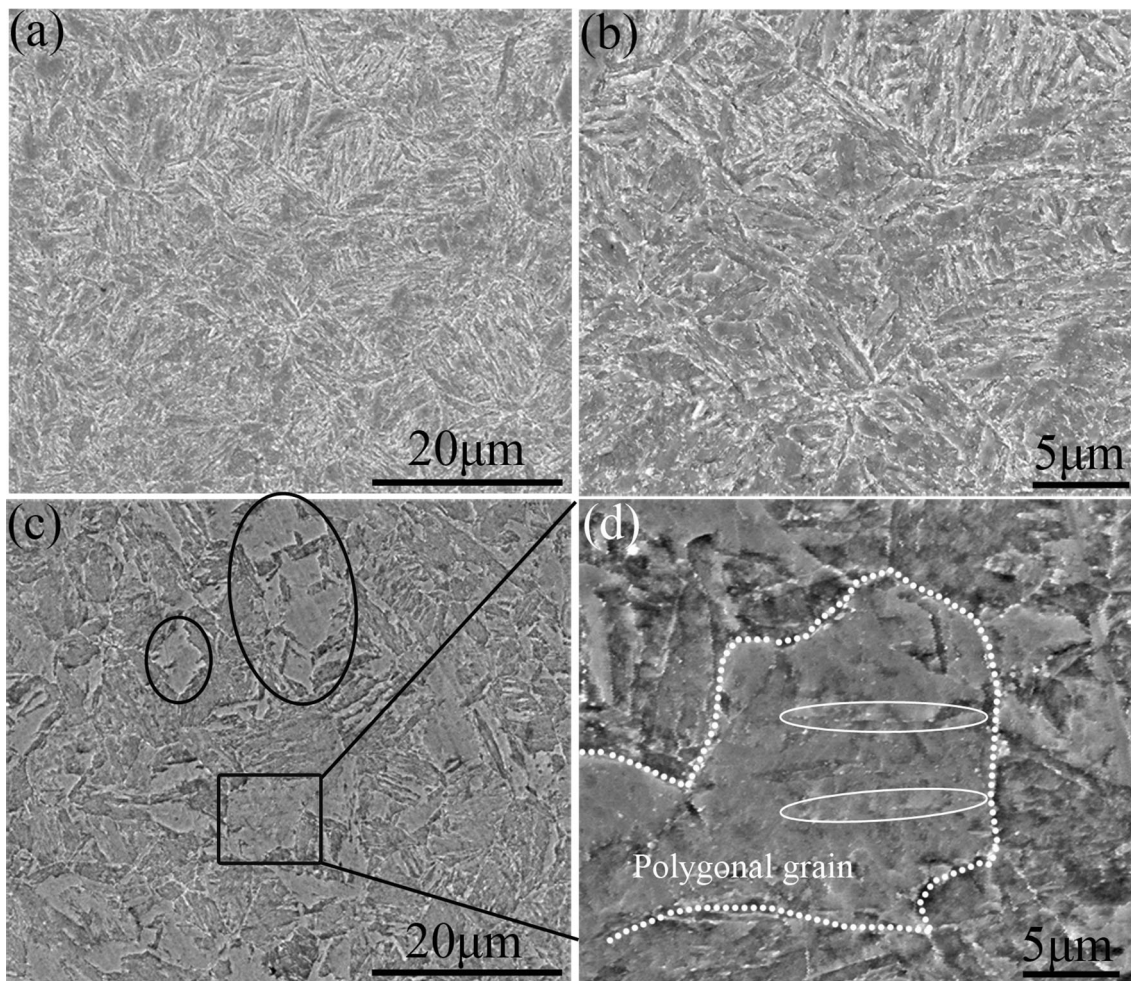


Fig. 6 Typical SEM images of tested samples quenched at 830 °C, DCT-treated and tempered at different temperatures: (a, b) F-sample; (c, d) I-sample

tempering are 580 and 540 °C, respectively, no notable differences in microstructure and morphology are observed for the K-sample, and its microstructures are basically identical to those of the sample tempered at 580 °C (F-sample) as shown in Fig. 3(c), still showing typical tempered martensitic structure. However, compared with the F-sample, the dislocation density within the martensitic laths of K-sample is somewhat reduced due to dislocation annihilations as shown in Fig. 9, but the martensitic lath width (Fig. 9b) and the grain size of carbides (Fig. 9c) and cannot be notably coarsened as the second tempering temperature (540 °C) is the lower than that of the first tempering temperature (580 °C).

3.3 Fracture Analysis

The fracture behaviors of the B-, C- and D-samples are similar with each other; hence, only the fractured B-sample was carried out for failure analysis for this group of samples. According to this method, the F-, J- and K-samples were also selected. All the experimental samples were fractured at room temperature tensile test, and subsequently SEM observations were performed on the fracture surfaces to further understand relationships between mechanical property and microstructures (Fig. 10).

As shown in Fig. 10(a) and (b), it can be seen that a large number of equiaxed dimples are observed in fracture surfaces of the B-sample, basically without the existence of tearing cracks, and some dimples connect to form coarse cracks (as shown the elliptic zone in Fig. 10b). This implies that the fracture mechanism of un-DCT-treated samples is ductile fracture. As shown in Fig. 10(c), the low-magnified rupture surfaces of the F-sample are different from those of the B-sample, mainly showing the dimples and some coarsely long-chain-like tearing cracks. Moreover, the fine long-chain-like tearing cracks are also observed in Fig. 10(d), and the fine tearing cracks are parallel to each other. The appearance of tearing cracks should be associated with the interfacial de-cohesion between soft α -Fe matrix and long-chain-like hard carbides. It has been demonstrated that during high-stress conditions and at the crack tip, the soft phase yield while the hard lath phases remain in the elastic state. The internal stresses at two-phase interfaces incompatibility increase by plastic deformation of the soft phase. As a result, when the shear stresses exceed the interfacial bonding strength, inevitably resulting in the appearance of interfacial de-cohesion. Later, at de-cohesive zones, the local stress concentration becomes much more evident, and crack propagations preferentially follow the

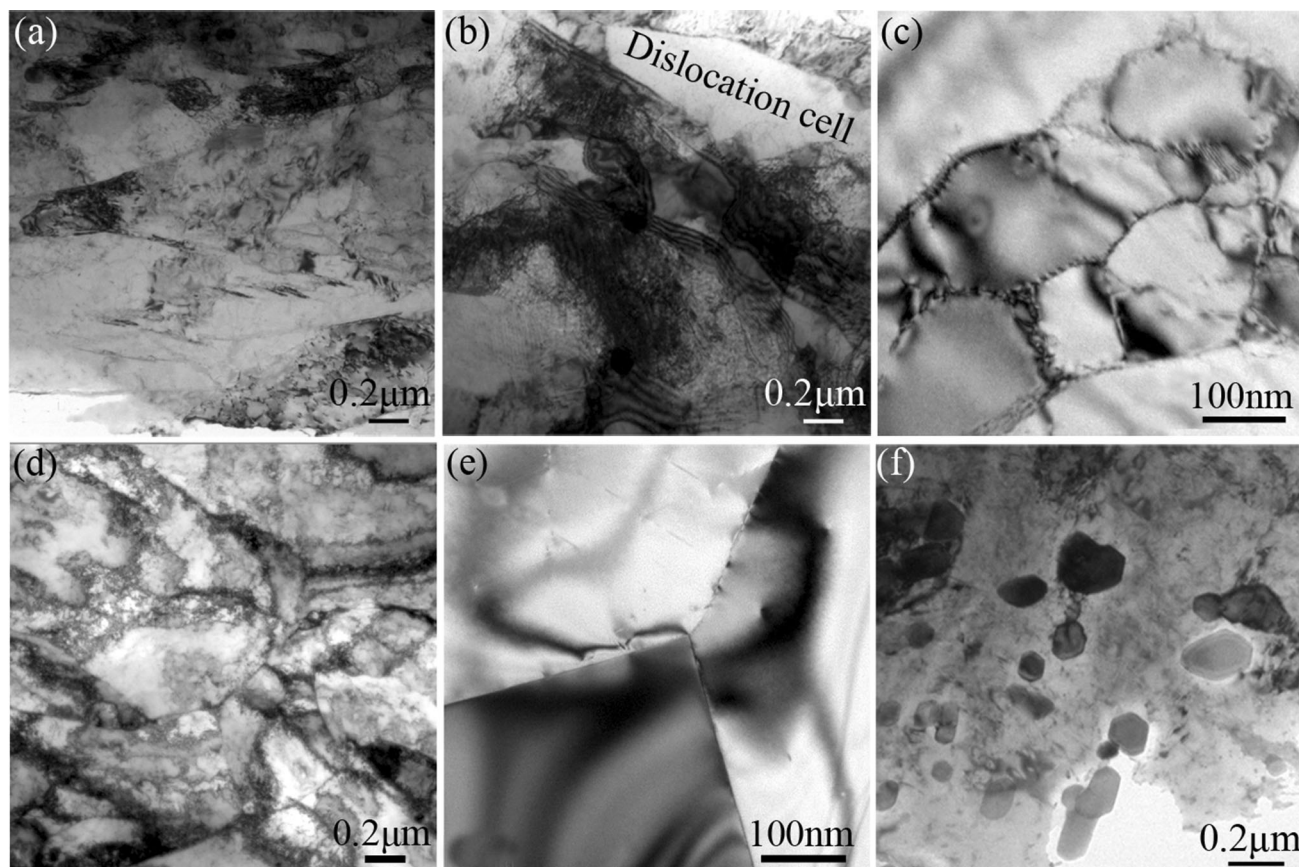


Fig. 7 Typical TEM images of a I-sample: (a) Lath morphology; (b, c) Recovery zones; (d, e) recrystallization zones; (f) carbides

two-phase interfaces, and finally produce numerous tearing cracks (Ref 26, 27). The similar interfacial de-cohesion was also observed at interfaces between hard phase and soft phase in a eutectic high-entropy alloy (Ref 28). Propagation speed of tear cracks is much faster than that of micropore aggregation cracks as the stress concentration much more easily occurs at the tearing crack tips. Hence, the existences of tearing cracks are claimed to be uncondusive to the material ductile and they are claimed as brittle-fracture feature. However, the dimples are claimed to be a feature of ductile fracture, and the formation of dimples involves plastic deformation. So the fracture mechanisms of DCT-treated samples belong to the mixed fractures of toughness and brittleness. As a result, the un-DCT-treated B-sample shows the higher fracture toughness when compared with the DCT-treated F-sample. The similar deformation mechanisms also occur in M-sample (Fig. 10e), but the number of tearing cracks in K-sample is the lower relative to the F-sample due to the reduction in dislocation density. A large number of coarse tearing cracks are observed in J-sample due to the appearance of interfacial cohesion between soft polygonal/equiaxed α -Fe grains and hard martensitic structures which result in uneven plastic deformation, and eventually failure of materials. As a result, the strength and hardness of J-sample are notably reduced.

3.4 Lifetime Measurements of Harmonic Drive Reducer

According to the results of property measurements and microstructural analysis, the F, G-, K- and L-samples were selected to fabricate the flex spline, and the B- and J-samples were selected for comparisons. In our statistical data, the

numbers of harmonic drive reducers with failures occurring in flex spline are calculated. Based on the experimental results, it shows that the average lifetimes of flex splines made of F-, G-, K- and L-samples are about 6170, 5800, 8640 and 7980 h respectively, whereas the ones of flex splines made of B- and J-samples are 4560 and 2950 h, less than the designed value (about 5000 h). Obviously, the DCT treatment in association with secondary tempering at special temperatures can effectively increase the lifetime of flex splines.

4. Discussion

It has been demonstrated in the present work that the mechanical properties are closely dependent on the microstructures which are controlled by heat treatment methods. The yield strength of steels associates with various strengthening effects, which are given in different terms in following equation (Ref 26):

$$\sigma_0 = \sigma_i + \sigma_g + \sigma_s + \sigma_{pct} + \sigma_p + \sigma_t \quad (\text{Eq 1})$$

where the σ_i is the lattice friction stress, for which $\sigma_i = 48 - 54$ MPa is commonly used for analysis of strengthening mechanisms in steels (Ref 29, 30), but in this work it = 50 MPa was used; σ_g is the grain-boundary strengthening; σ_s is the solid solution strengthening due to carbon content and other alloying elements; σ_{pct} is the precipitation strengthening; σ_p is dislocation strengthening; and σ_t is the crystallographic texture strengthening, here $\sigma_t = 0$ because the texture is not formed in this work.

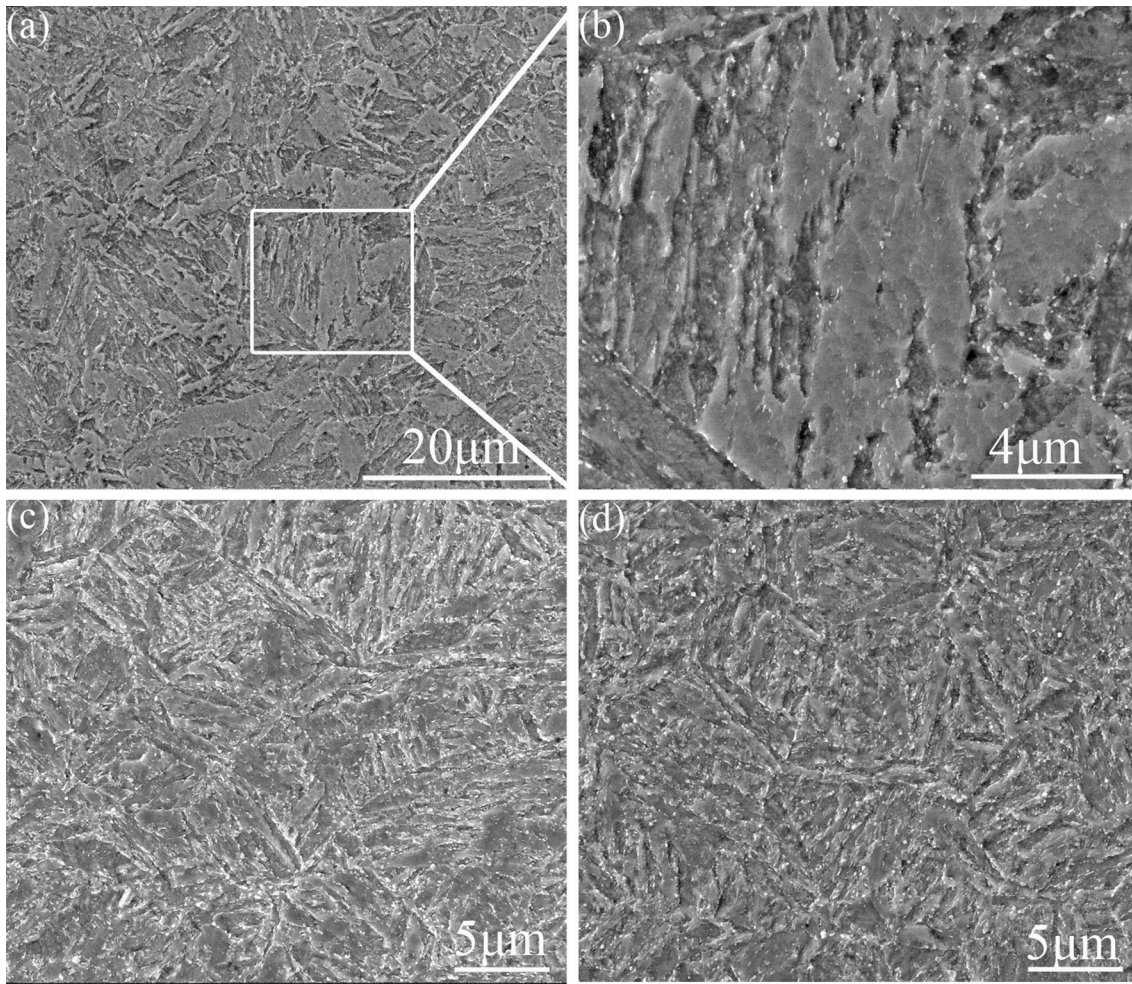


Fig. 8 Typical microstructures of quenched and tempered samples with DCT: (a) 850, 580 and 580 °C; (b) 850, 580 and 540 °C; (c) 830, 580 and 540 °C

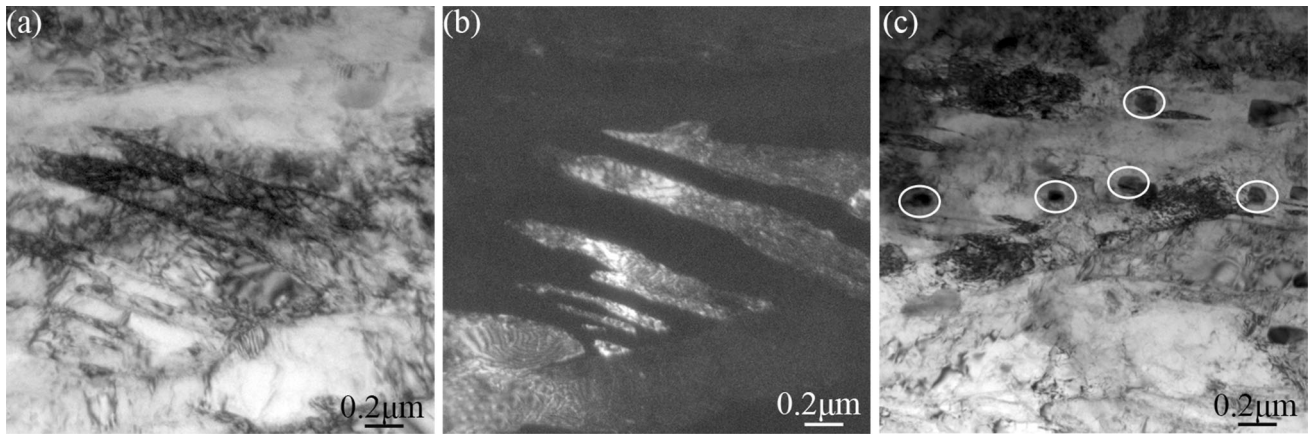


Fig. 9 Typical TEM images of a K-sample: (a) bright-field image; (b) centered dark-field image of (a); (c) carbides

The σ_g is expressed by the conventional H-P formula (Ref 31, 32):

$$\sigma_g = K_{HP}d^{-0.5} \quad (\text{Eq 2})$$

where d is the mean grain size, K_{HP} is coefficient for steel taken $0.6 \text{ MPa}\cdot\text{m}^{-0.5}$ (Ref 31, 32).

The σ_s is determined by concentration of solutes (Ref 33):

$$\sigma_s = k_i c_i \quad (\text{Eq 3})$$

where k_i is the strengthening coefficient, and c_i is the concentration of solute i , wt pct.

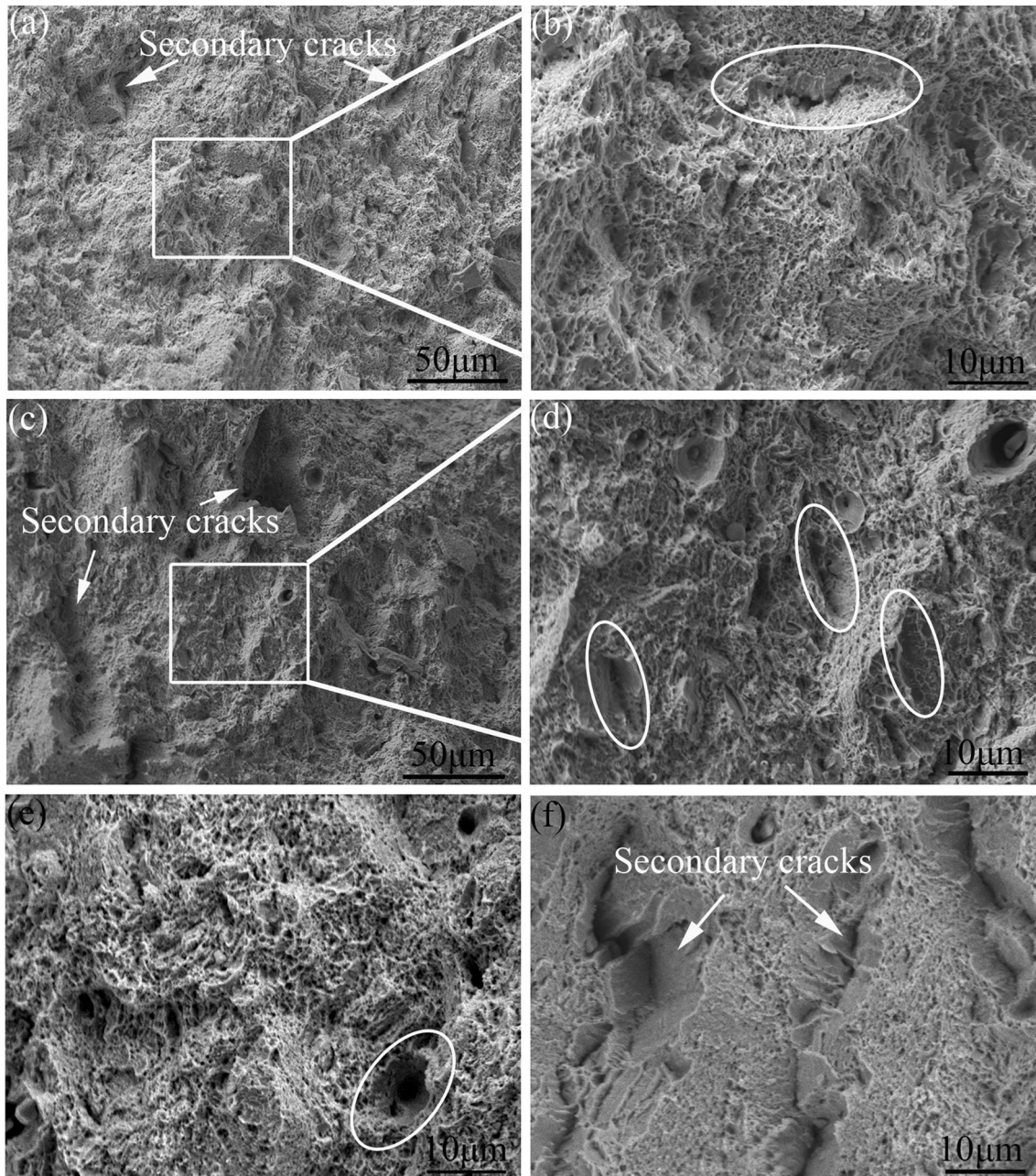


Fig. 10 Typical SEM images of tensile fracture surface of the tested samples fractured at room temperature: (a) B-sample; (b) magnified image of the framed zone in (a); (c) F-sample; (d) magnified image of the framed zone in (c); (e) K-sample; (f) J-sample

The σ_{pct} can be used the Ashby-Orowan relationship (Ref 34):

$$\sigma_{pct} = (0.538Gb f^{0.5} d^{-1}) \ln\left(\frac{d}{2b}\right) \quad (\text{Eq 4})$$

where the shear modulus $G = 81.6\text{GPa}$, the Burgers vector $b = 0.248\text{ nm}$, f and d are the volume fraction and size of precipitates, respectively.

The σ_p can be obtained using the Bailey-Hirsch relation (Ref 35, 36):

$$\sigma_p = \alpha M b G \rho^{0.5} \quad (\text{Eq 5})$$

where α is a constant, and M is the Taylor factor, ρ is the dislocation density, and the $\rho = 0.96 \times 10^{15}\text{ m}^{-2}$ for quenched and tempered sample (Ref 37). The value $\alpha \times M$ for Fe was experimentally estimated to be 0.5 (Ref 37).

In order to illustrate the contributions from strengthening mechanisms to yield stress, a group of samples (taking the B-, F- and G-samples for example) were carried out. For the B- and F-samples, the solubility of carbon atom in for quenched and tempered samples with and without DCT treatment is 0.0218 and 0.06 wt.% [f]. So the σ_s values of the samples with and without DCT treatment are 71 and 26 MPa in this work, respectively. The grain sizes of prior austenite of both B- and F-samples are 11.3 μm due to the same quenching process. The

Table 3 Contributions from different strengthening mechanisms

Treatment	Calculated data, MPa						Experimental data, MPa YS
	σ_i	σ_g	σ_s	σ_{pct}	σ_p	σ_t	
B-sample	50	178	71	558	314	0	919.2
F-sample	50	178	26	1527	>314	0	988.8
K-sample	50	178	26	1527	<314	0	950.8

percentages of carbides in B- and F-samples have been estimated to be equal to 1.09 and 2.95 wt.%, and the sizes of carbides of them are 0.11 and 0.06 μm by statistically measurements of at less 500 carbides. Because the secondary tempering temperature of the G-sample is 540 $^{\circ}\text{C}$, the lower than the first tempering temperature (540 $^{\circ}\text{C}$), it can be claimed that the secondary tempering cannot have a basic effect on the carbon solubility, grain size, as well as the percentage and size of carbides. So the carbon solubility, grain size, as well as the percentage and size of carbides are 0.0218 wt.%, 11.3 μm , 2.95 wt.% and 0.06 μm . But the secondary tempering can effectively reduce the dislocation density which has been confirmed by TEM observations (Fig. 7 and 9).

The calculated contributions from strengthening mechanisms to yield strength are shown in Table 3. It can be found that the calculated data does not completely coincide with experimental data for both the B- and F-samples. The differences in calculated and experimental data are due to complex interaction of strengthening mechanisms in steels, especially between grain-boundary strengthening, precipitation strengthening and dislocation strengthening. However, analysis of strengthening mechanisms confirms that the yield strength of the B-sample is ensured basically by grain boundaries, precipitate and dislocations, but precipitate strengthening is dominant. (When the percentage of carbides is increased by about 1%, the yield strength is increased by about 500 MPa in theory). For the B-, C- and D-samples, its yield strength is mainly controlled by precipitate strengthening mechanism. So there are notable differences in yield strength of the B-, C- and D-samples. For the F-sample, the DCT promotes the transformation of retained austenite to martensite, the refinement of martensitic substructures and the precipitation and even distribution of θ -phase carbides. Hence, the F-sample shows the yield strength compared with B-sample (Table 2). Further secondary tempering at controllable temperatures (ranging from 540-580 $^{\circ}\text{C}$) reduces the dislocation density of materials, resulting in an increase in ductility but a somewhat loss in yield strength. This is why the K-sample (or M-sample) shows a lower strength but a higher ductility compared with the F-sample (or G-sample). Higher secondary tempering (≥ 580 $^{\circ}\text{C}$) promotes the formation of both polygonal and equiaxed grains with low hardness, leading to a notable loss in yield strength. This is why the J-sample reveals a lower strength in comparison to the K-sample.

5. Conclusions

Based on the above-mentioned property measurements and microstructural characterizations, the following can be concluded:

1. For QT-treated samples, the DCT effectively promotes the transformation of retained austenite to martensite, the refinement of martensitic substructures and the precipitation and even distribution of θ -phase carbides, resulting in a notable increase in hardness, yield strength and tensile strength, but a slight loss in elongation and impact energy.
2. Secondary tempering at special temperatures can successively increase the elongation and fracture toughness of the DCT-treated 40CrNiMoA steels at the cost of slight decrease in hardness and strength.
3. The DCT in combination with secondary tempering at 540-580 $^{\circ}\text{C}$ can effectively improve the comprehensive mechanical properties of 40CrNiMoA steel, and further ensure the flex spline with a higher lifetime.

Acknowledgments

This work was supported by the Key Research Project of Jiangxi Province (20161BBE50064, 20171BBH80011).

References

1. L. Anthony (2006). The basics of Harmonic Drive Gearing. Gear Product News, pp. 32–36
2. S. Zhirafar, A. Rezaeian, and M. Pugh, Effect of Cryogenic Treatment on the Mechanical Properties of 4340 Steel, *J. Mater. Process. Technol.*, 2007, **186**, p 298–303
3. J.Y. Huang, Y.T. Zhu, X.Z. Liao, I.J. Beyerlein, M.A. Bourke, and T.E. Mitchell, Microstructure of Cryogenic Treated M2 Tool Steel, *Mater. Sci. Eng. A*, 2003, **339**, p 241–244
4. V. Firouzdor, E. Najati, and F. Khomamizadeh, Effect of Deep Cryogenic Treatment on Wear Resistance and Tool Life of M2 HSS Drill, *J. Mater. Process. Technol.*, 2008, **206**, p 467–472
5. H.G. Nanesa, M. Jahazi, and R. Naraghi, Martensitic Transformation in AISI, D2 Tool Steel, *J. Mater. Sci.*, 2015, **50**, p 5758–5768
6. M. Pérez and F.J. Beizunce, The Effect of Deep Cryogenic Treatments on the Mechanical Properties of an AISI, H13 Steel, *Mater. Sci. Eng. A*, 2015, **624**, p 32–40
7. P. Baldissera, Deep Cryogenic Treatment of AISI, 302 Stainless Steel: Part I, Hardness and Tensile Properties, *Mater. Des.*, 2010, **31**, p 4725–4730
8. J.D. Darwin, D. Mohan Lai, and G. Nagarajan, Optimization of Cryogenic Treatment to Maximum the Wear Resistance of 18% Cr Martensitic Stainless Steel by Taguchimethod, *J. Mater. Process. Technol.*, 2008, **195**, p 241–247
9. M. Preciado and M. Pellizzari, Influence of Deep Cryogenic Treatment on the Thermal Decomposition of Fe-C Martensite, *J. Mater. Sci.*, 2014, **49**, p 8183–8191
10. A. Akhbarizadeh, A. Shafyei, and M.A. Golozar, Effects of Cryogenic Treatment on Wear Behavior of D6 Tool Steel, *Mater. Des.*, 2009, **30**, p 3259–3264

11. R. Thornton, T. Slatter, and H. Ghadbeigi, Effects of Deep Cryogenic Treatment on the Dry Sliding Wear Performance of Ferrous Alloys, *Wear*, 2013, **305**, p 177–191
12. A. Bensely, L. Shyamala, S. Harish, D. Mohan Lai, G. Nagarajan, K. Junik, and A. Rajadurai, Fatigue Behavior and Fracture Mechanism of Cryogenically Treated En 353 steel, *Mater. Des.*, 2009, **30**, p 2955–2962
13. D. Das, A.K. Dutta, and K.K. Ray, Sub-Zero Treatments of AISI, D2 Steel: Part I. Microstructure and Hardness, *Mater. Sci. Eng. A*, 2010, **527**, p 2182–2193
14. D. Das, K.K. Ray, and A.K. Dutta, Influence of Temperature of Sub-Zero Treatments on Wear Behavior of Die Steel, *Wear*, 2009, **267**, p 1361–1370
15. S.H. Li, N. Min, J.W. Li, X.C. Wu, C.H. Li, and L.L. Tang, Experimental Verification of Segregation of Carbon and Precipitation of Carbides Due to Deep Cryogenic Treatment for Tool Steel by Internal Friction Method, *Mater. Sci. Eng. A*, 2013, **575**, p 51–60
16. Z.H. Wan, H. Hao, H. Zhou, S.N. Gou, H.J. Hu, L.M.C. Yang, K.F. Zhang, Performance and Testing of Harmonic Drive Gears Lubricated with Two Types of Lubrication: Liquid-Lubrication H-DLC-Coating and Solid MoS₂, 15th European Space Mechanisms @ Tribology Symposium-ESMATS 2013, Noordwijk, The Netherlands, 25-27 September 2013
17. ASTM E975-00: Standard Practice for X-ray Determination of Retained Austenite in Steel with Near Random Crystallographic Orientation, vol. 0301., ASTM book of standard, West Conshohocken, PA, United States, 2004
18. H. Kitahara, R. Ueki, N. Tsuji, and Y. Minamino, Crystallographic Features of Lath Martensite in Low-Carbon Steel, *Acta Mater.*, 2006, **54**, p 1279–1288
19. C.Y. Zhang, Q.F. Wang, J.X. Ren, R.X. Li, M.Z. Wang, F.C. Zhang, and K.M. Sun, Effect of Martensitic morphology on Mechanical Properties of an As-quenched and Tempered 25CrMo48V Steel, *Mater. Sci. Eng. A*, 2012, **534**, p 339–346
20. J.H. Shim, H.J. Lee Voigt, and B.D. Wirth, Temperature Dependent Dislocation Bypass Mechanism for Coherent Precipitates in Cu-Co Alloys, *Acta Mater.*, 2016, **110**, p 276–282
21. M. Askari-Paykani, H.R. Shahverdi, and R. Miresmaeili, Microstructural Evolution and Mechanical Properties of a Novel FeCrNiBSi Advanced High-Strength Steel: Slow, Accelerated and Fast Casting Cooling Rate, *Mater. Sci. Eng. A*, 2016, **668**, p 188–200
22. H.K.D.H. Bhadeshia, R.W.K. Honeycombe, *Steel: Microstructure and Properties* (4th edition), 2017, pp. 237–270
23. X.N. Meng, C. Li, and W.L. Chen, Effects of Ti and B Addition on Microstructures and Mechanical Properties of Hot-Rolled High-Strength Nb-Containing Steels, *J. Mater. Eng. Perform.*, 2016, **25**, p 3472–3481
24. A. GhateiKalashami, A. Kermanpur, E. Ghassemali, A. Najafzadeh, and Y. Mazaheri, Correlation of Microstructure and Strain Hardening Behavior in the Ultrafine-Grained Nb-Bearing Dual Phase Steels, *Mater. Sci. Eng. A*, 2016, **678**, p 215–226
25. J. Sobotova, P. Jurci, and I. Dlouhy, The Effect of Subzero Treatment on Microstructure, Fracture Toughness, and Wear Resistance of Vanadis 6 Tool Steel, *Mater. Sci. Eng. A*, 2016, **652**, p 192–204
26. F.B. Pickering, *Materials Science and Technology: A Comprehensive Treatment, Constitution and Properties of Steels*, Vol 7, VCH, Weinheim, 1992
27. I. Gutierrez, Modeling the Mechanical Behavior of Steels with Mixed Microstructures, *Metalurgija-J. Metall.*, 2005, **11**, p 201–214
28. P. Phetlam and V. Uthaisangskuk, Microstructure Based Flow Stress Modeling for Quenched and Tempered Low Alloy Steel, *Mater. Des.*, 2015, **82**, p 189–199
29. Y.L. Kang, Q.H. Han, X.M. Zhao, and M.H. Cai, Influence of Nanoparticle Reinforcements on the Strengthening Mechanisms of an Ultra-Fine-Grained Dual Phase Steel Containing Titanium, *Mater. Des.*, 2013, **44**, p 331–339
30. J. Lu, Q. Omotoso, J.B. Wiskel, D.G. Ivey, and H. Henein, Strengthening Mechanisms and their Relative Contributions to the Yield Strength of Microalloyed Steels, *Metal. Mater. Trans.*, 2012, **43A**, p 3043–3061
31. R. Shukla, S.K. Das, B.R. Kumar, S.K. Ghosh, S. Kundu, and S. Chatterjee, An Ultra-Low Carbon, Thermomechanically Controlled Processed Microalloyed Steel: Microstructure and Mechanical Properties, *Metal. Mater. Trans.*, 2012, **43A**, p 4835–4845
32. S. Takaki, K. Kawasaki, and Y. Kimura, Mechanical Properties of Ultra Fine Grained Steels, *J. Mater. Process. Technol.*, 2001, **117**, p 359–363
33. S. Schmauder and C. Kohler, Atomistic Simulations of Solid Solution Strengthening of α -Iron, *Comput. Mater. Sci.*, 2001, **50**, p 1238–1243
34. T. Gladman, Precipitation Hardening in Metals, *Mater. Sci. Technol.*, 1999, **15**, p 30–36
35. J.E. Bailey and P.B. Hirsch, The Dislocation Distribution, Flow Stress, and Stored Energy in Cold-Worked Polycrystalline Silver, *Philos. Mag.*, 1960, **5**, p 485–497
36. B.Q. Han, E.J. Lavernia, and F.A. Mohamed, Dislocation Structure and Deformation in Iron Processed by Equal-Channel-Angular Pressing, *Metal. Mater. Trans.*, 2004, **35A**, p 1343–1350
37. R.K. Islamgaliev, M.A. Nikitina, A.V. Ganeev, and V.D. Sitdikow, Strengthening Mechanisms in Ultrafine-Grained Ferritic/Martensitic Steel Produced by Equal Channel Angular Pressing, *Mater. Sci. Eng. A*, 2019, **744**, p 163–170

Publisher's Note Springer Nature remains neutral with regard to jurisdictional claims in published maps and institutional affiliations.